

# Analysis of the Keyhole and Weld Pool Dynamics by Imaging Evaluation and Photodiode Monitoring

Alexander F. H. KAPLAN, Peter NORMAN and Ingemar ERIKSSON

Luleå University of Technology, SE-97 451 Luleå, Sweden; Homepage: [www.ltu.se/tfm/produktion](http://www.ltu.se/tfm/produktion)  
e-mail: [alexander.kaplan@ltu.se](mailto:alexander.kaplan@ltu.se)

Process monitoring of laser welding defects by commercial systems based on photodiodes has high potential, but improved understanding is desirable for more systematic industrial use. The signal is generated from spectrally filtered emissions or reflections from the dynamic welding process. Improved knowledge on the cause of the signal was achieved by accompanying high speed imaging. Numerical evaluation of the images and subsequent modelling provided additional information to judge the potential and limits of commercial photodiode sensors. For welding with a 3 kW Nd:YAG-laser, a 15 kW fibre laser or a 14 kW CO<sub>2</sub>-laser, various joint cases were studied with respect to defects like craters, spatter, blowholes, underfill, root drop-out, lack of penetration, lack of fusion or pores. From the findings a more general theoretical description of the links between the welding process, the defect mechanism and the generated signal was initiated.

**Keywords:** laser welding, defect, quality, process monitoring, photodiode, imaging, model, keyhole

## 1. Introduction

Laser welding has high industrial potential, both in product development and production. However, this potential can only be released when the targeted function, mainly the mechanical properties, can be achieved and guaranteed. This corresponds to the suppression of any unacceptable welding defects. While post-process inspection is often associated with large expenses and limited reliability, on-line monitoring (not control loops, being a more complex task) of defects basically would be a highly efficient method with limited costs. A few monitoring systems are nowadays commercially available, mainly either based on cameras observing the weld pool and keyhole or photodiodes detecting the radiation emitted or reflected from the interaction zone. However, these systems suffer from certain disadvantages so far. Camera-based systems require powerful and robust image-processing, often case-dependent. Monitoring systems relying on photodiodes (which are studied in the present paper) apply empirical rules, thus the applicability of a system is often unpredictable, lacking a systematic strategy. Research on process monitoring was carried out at different levels, often either to associate mechanisms with a certain defect and signal for a specific case or for developing improved systems and algorithms. Comprehensive reviews on process monitoring of laser materials processing were accomplished [1-3].

Goal of the present study is improved understanding of the potential and limits of the applicability of commercial photodiode-based systems. For this purpose analysis was conducted at different levels for a series of industrial cases. Eventually, a generalised theory with guidelines is aimed at.

## 2. Methodology

Nine different industrial welding cases have been studied so far, moreover some fundamental welding experiments were conducted. The cases chosen vary significantly from each other to accomplish a wide spectrum of joint

types, dimensions, materials, defects, etc., with the expectation to represent wide areas of applications.

For process monitoring the Precitec LWM system was chosen, equipped with three photodiode sensors, Fig. 1(a), that can be applied simultaneously to detect different wavelength spectra, namely 400-600 nm (as an indication called the "Plasma" sensor P), 1060-1070 nm (the laser "Reflection" sensor R) and 1100-1800 nm (the "Temperature" sensor T). A sampling frequency up to 20 kHz can be achieved. As illustrated in Fig. 1(a), the optical path of the sensors is arranged concentric to the near IR-laser optics. For CO<sub>2</sub>-laser applications the sensors were employed externally.

For improved understanding of the link between the welding process and the acquired signals, all experiments were accompanied by high speed imaging, see Fig. 1(a), along with an illumination diode laser (whenever advantageous). The cameras had a bandpass filter of 810±2 nm. In some experiments the process was observed simultaneously with and without illumination, providing more information. For some cases the images were quantitatively evaluated, enabling deeper analysis and subsequent modelling.

A typical high speed image with low illumination is shown in Fig. 1(b), enabling to observe beside the keyhole also the vapour plume. Note that the sensor detects a surface area with a radius of about 5 mm around the beam axis, thus not necessarily the rear part of the melt pool, see Fig. 1(c). From the geometrical facts identified from high speed images, for some cases the thermal emissions to the sensor, see Fig. 1(d), were modelled [4] in order to analyse the T-signal (neglecting the vapour so far). This required to divide into four regions of different emissivity, see Fig. 1(c). The signal is the integration over all rays hitting the sensor.

A much more detailed description of the different cases studied and of the accompanying experimental and theoretical methods can be found in corresponding publications [5-9]. In contrast, the present paper gives a survey and tries to derive a generalised theory with guidelines.

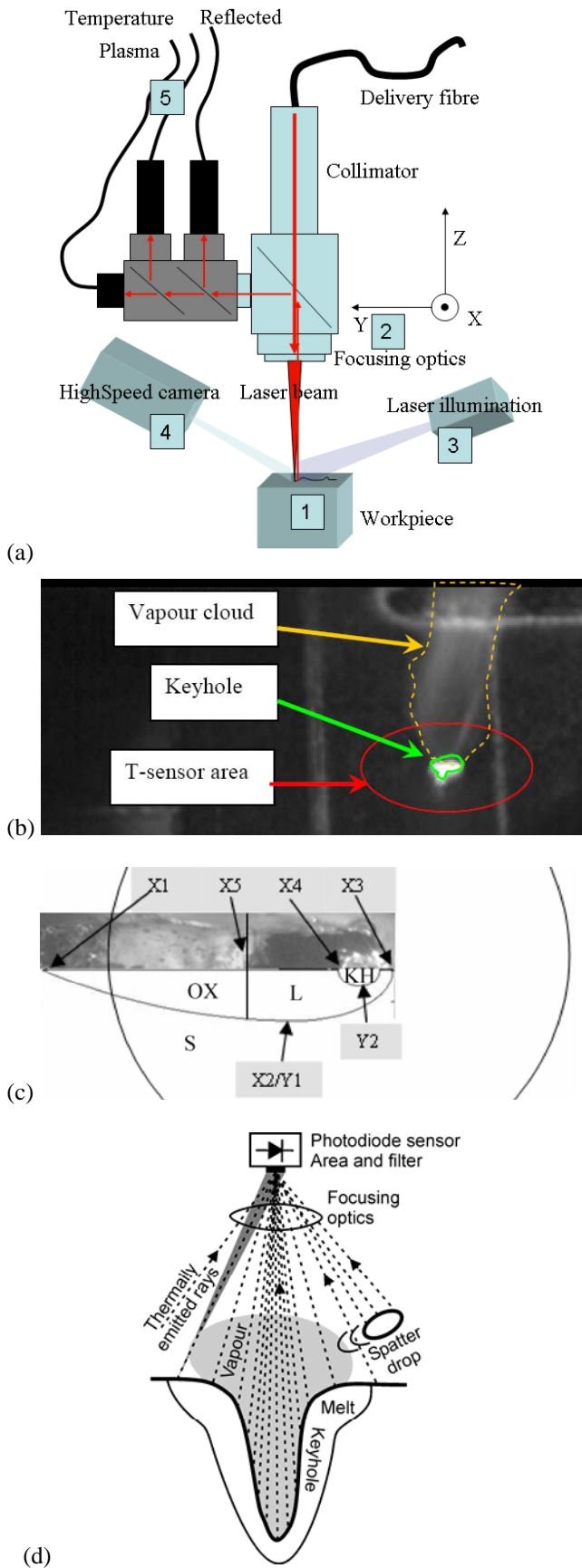


**Fig. 1** Method; (a) experimental monitoring and imaging set-up, (b) sensor area with radiating keyhole and vapour, (c) pool areas of different emissivity: KH keyhole, L blank liquid, OX oxide, S solid, (d) keyhole and melt pool cross section with the emission contributions to the sensor

### 3. Results and discussion of different cases

Only a selection [5-9] of the nine cases is presented here.

#### 3.1 Case 1: Blowouts, undercut and root drop-out

Case 1 is a butt joint (tubes with milled edges) of 12 mm thickness, joining S420MC-steel with 25CrMo4-steel, welded with a 14 kW CO<sub>2</sub>-laser [5]. The sequence of high speed images in Fig. 2(a)-(h) shows the temporary sagging down of the weld at the top (and in turn at the root), causing an undercut. A weld cross section with undercut and root drop-out (and pore formation) can be seen in Fig. 3(g), while Fig. 3(h) shows a good top shape, but again root sagging. Figures 3(a)-(f) show the top weld appearance of a good weld compared to an undercut and a blowout, accompanied by typical high speed images. The images show that for blowouts the mechanism is faster than for undercuts.

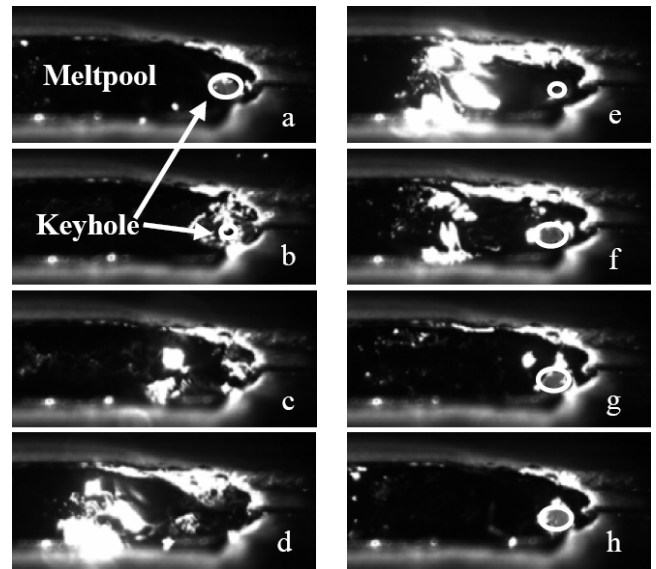


**Fig. 2** Sequence (steps: 1 ms) of high speed images showing a temporary melt top sagging wave causing an undercut

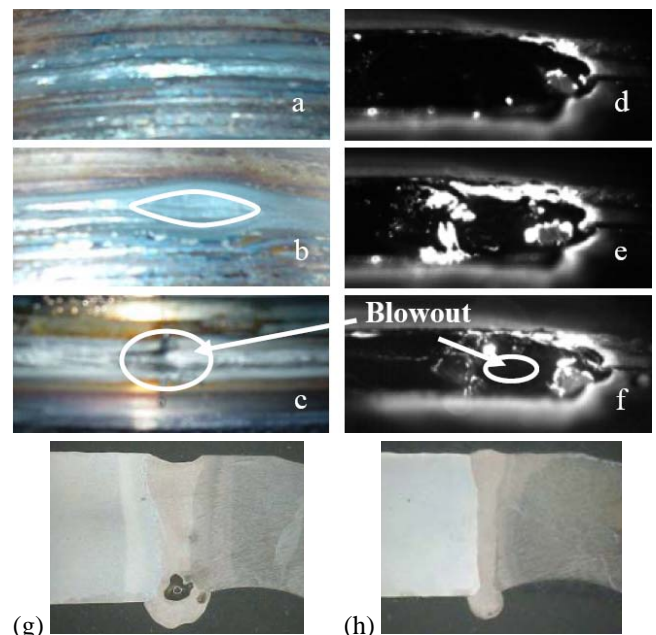


**Fig. 3:** Weld top surface appearance and high speed images: (a),(d) good weld, (b),(e) undercut, (c),(f) blowout; weld cross section (g) with undercut, (h) only root sagging

Corresponding P-signals are shown in Fig. 4. The teach-in signal for a good weld and its corresponding alert thresholds are shown in Fig. 4(a), while Figs. 4(b)-(e) show the signals for blowout and undercut that are once detected with these thresholds, once not (although visible).

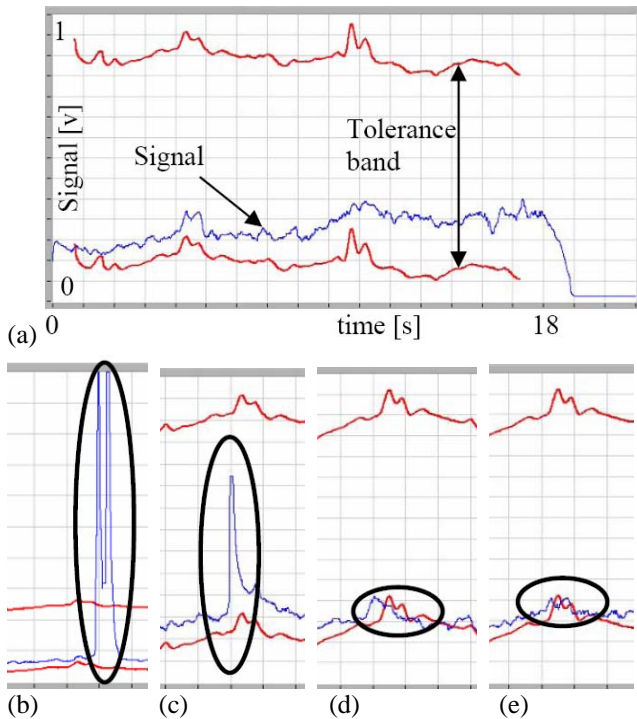


**Fig. 4** Monitoring signal  $U(t)$  with taught upper and lower limit: (a) good weld (reference), (b) detected blowout (note: different vertical scale), (c) undetected small blowout, (d) detected undercut, (e) undetected small undercut

From high speed imaging it was seen that the blowout mechanism is a fast phenomenon. When the blowout takes place in the pool it has less impact on the keyhole and metal vapour, which mainly compose the signal. Thus smaller blowouts can have a too weak signal change. Even weaker are undercut signals, but they narrow keyhole, lasting e.g. 2 s. Again smaller size is more difficult to detect.

### 3.2 Case 2: Craters for overlapping Zn-coated steel

In Case 2 the well known phenomenon of spatter and crater formation (blowouts) due to Zn-boiling in confined overlap condition is studied [6]. Figure 5(a) shows one of the four types of joint configurations studied. The top surface appearance of a defect-free weld is shown in Fig. 5(b) while Fig. 5(c) shows the location of blowouts along the weld that were classified into 3 modes after high speed imaging analysis, see Fig. 6(a)-(r). The signal of the T- and R-sensor correlated to the blowout locations is shown in Fig. 6(s). Some of the bubble breakthroughs happen in the melt pool, while others emerge from the keyhole.

No obvious correlation was identified despite the severe, clearly visible surface dynamics during the crater formation. One hypothesis is that part of the event can happen outside the sensor range, another is that dynamics in the pool causes less emission dynamics than the keyhole. The latter is much more sensitive by changing its opening size, proportionally changing its high radiation contribution.

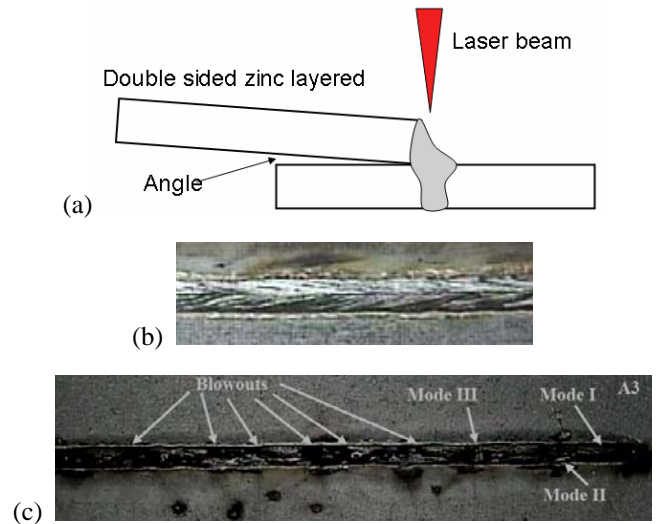


**Fig. 5** Zn-coated steel in overlap position: (a) one of the four studied joint configurations, (b) good weld surface, (c) weld surface with blowholes and spatter deposition

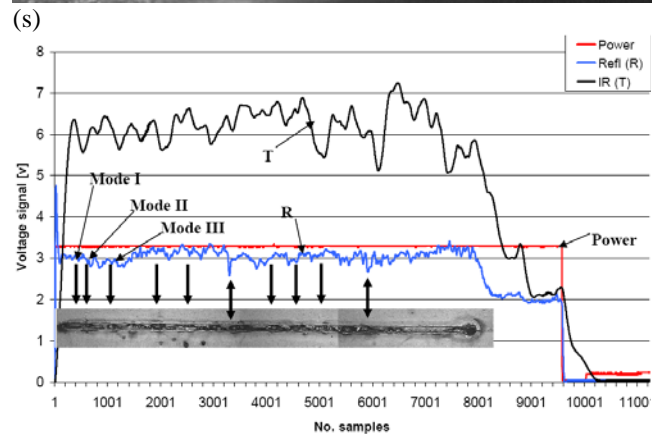
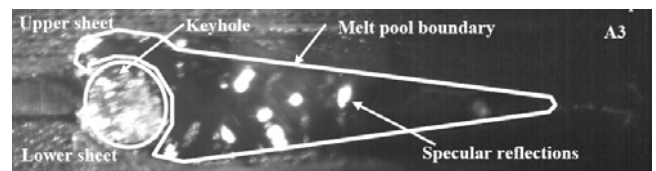
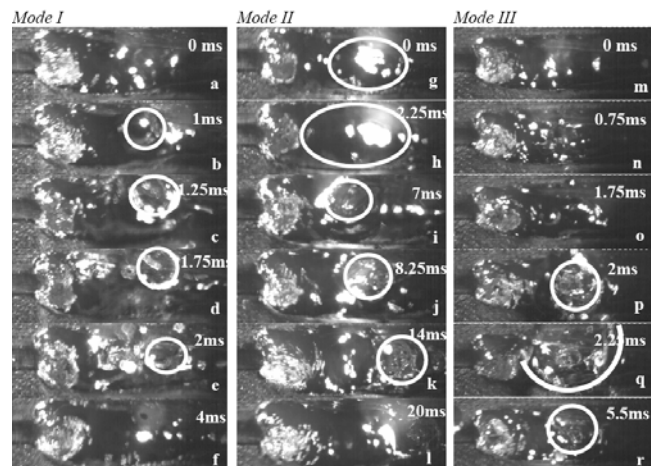


**Fig. 6** (a)-(r) High speed image sequences of 3 modes of blowouts, (s) image explanation with joint edge, keyhole, weld pool, (t) T- and R-sensor signal correlated to blowouts

### 3.3 Case 3: High brightness lasers: spatter, underfill

When welding 8 mm thick stainless steel SS 304 with a 15 kW fibre laser beam [7] even at moderate focusing conditions spatter and underfill is likely to take place, see Fig.7 (here: spot diameter: 400  $\mu\text{m}$ , Rayleigh length:  $\pm 4$  mm, power density up to 12 MW/cm<sup>2</sup> but via focal plane varied).

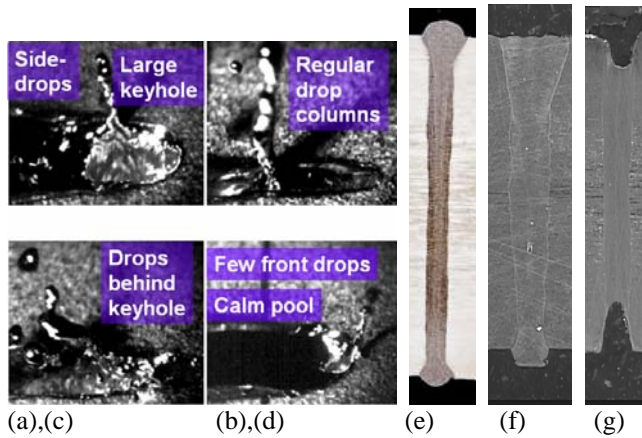


**Fig. 7** High speed images: (a)-(d) Modes I-IV of spatter ejection; Cross section : (e) 16 mm and (f) 8 mm acceptable weld, (g) underfill at top and root (8 mm)

From high speed imaging four different modes of spatter could be distinguished, see Fig. 7(a)-(d). From advanced high speed imaging analysis statistical properties can be measured, see Tab. 1, that characterize the apparently different behaviour of the four modes. While for welding with 15 kW beam power (7 m/min) it was difficult (Mode II, focus at the surface, see Fig. 7(b),(g)) to achieve welds free of spatter and underfill (although spatter became less severe for defocusing, Modes I,III), welding with 7.5 kW (Mode IV) but same line energy (reduced speed: 3 m/min) gave highly stable welding without underfill and with little spatter, see Fig. 7(d),(f). In contrast to Modes I-III, Mode IV has high drop speed, but low drop frequency, volume and angle. One explanation might be wider pool geometry.

**Table 1** Average drop properties for the four spatter modes

Mode	Frequency [Hz]	Volume [mm <sup>3</sup> /ms]	Speed* [m/s]	Angle* [°]	Energy [10 <sup>-8</sup> J/s]
I	424	105	1.63	48	4.7
II	737	388	1.45	61	41.5
III	1000	427	1.62	71	41.0
IV	196	5	3.05	4	1.7

\* average per drop, otherwise accumulated per second

Figure 8(a) shows the measured drop speed as a function of the drop volume for the four different modes, clearly showing the high speed/low volume character of Mode IV. From speed and volume the kinetic energy can be derived, see Fig. 8(b), and compared to the surface tension energy (creating new surface area per drop). The latter turns out to be one order of magnitude larger. So imaging, its evaluation and subsequent calculation provides additional information supporting analysis. Monitoring was not yet applied here.

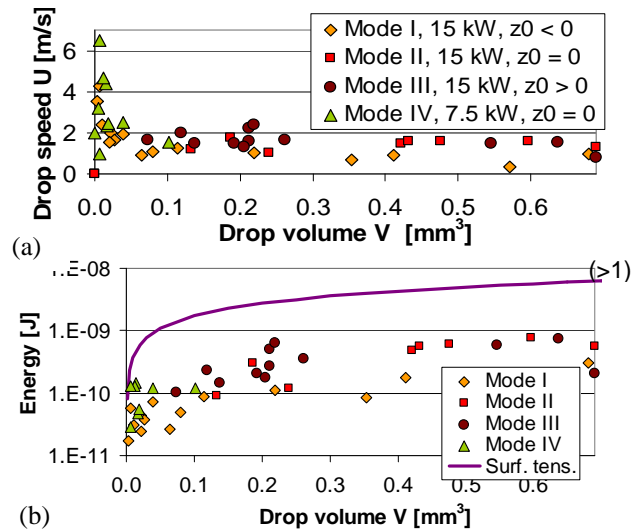


**Fig. 8** Evaluation of high speed imaging for the 4 modes: (a) drop speed as a function of drop volume, (b) kinetic and surface tension energy as a function of drop volume [7]

### 3.4 Case 4: Overlap weld width as quality criterion

Another case studied [8] has the width of an overlap weld at the interface as criterion. For increasing speed the depth of penetration and the weld width decrease, as can be expected, see Fig. 9(a),(b). The T-signal, see Fig. 9(d), decreases correspondingly for increasing speed, however, with a peak at 4 m/min, where also the weld pool is longest, see Fig. 9(b),(c) (perhaps due to favourable absorption conditions). Due to modelling of the emissions based on the weld pool dimensions, see the bars in Fig. 9(d), it was shown that both the decay (for increasing speed) and the peak in the signal can be explained through the combination of pool width and length governing the emissions. So although the T-sensor is rather insensitive to melt pool dynamics, it well detects the pool size or the associated temperature field.

### 3.5 Case 5: Humping

For similar parameters humping took place [8], correlating fully in time with the sensor signal maxima, see Fig. 11(a). For this case the model did not correlate sufficiently with the experiments to explain the mechanisms, see Fig. 11(d), thus certain assumptions need further improvement. Nevertheless, from high speed imaging can be clearly observed and measured that a series of geometrical properties and mechanisms oscillate with the same frequency as the humps. From this we conclude that the weld pool itself can be regarded as an oscillating system with a certain eigenfrequency causing the humps, while the keyhole oscillated at higher frequencies, see Fig. 10(a),(b) that were not detected by the sensor, particularly as it applied a default digital low pass filter.

Humping would have been expected to be difficult to detect, as being a pool motion with low impact on the signal. The interpretation is still unclear, as the hypothesis that the harmonic oscillating generates the signal was not confirmed by the model (phase shift), while the hypothesis on a corresponding keyhole motion can only partially be confirmed (moving average shows similarities), as it experiences faster motions.

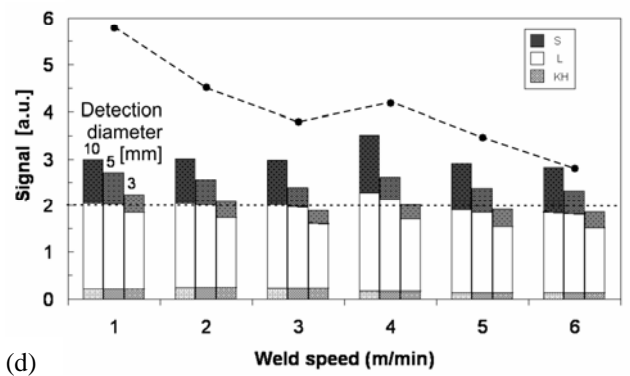
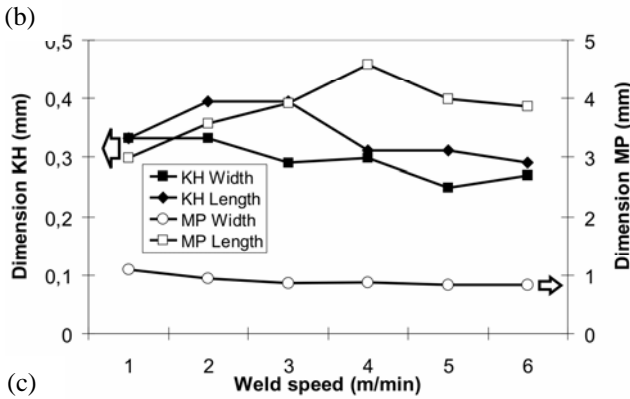
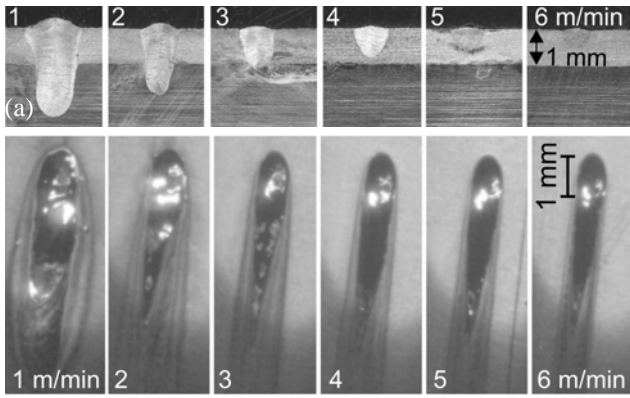


Fig. 9 Analysis of the weld width as detection criterion [8]

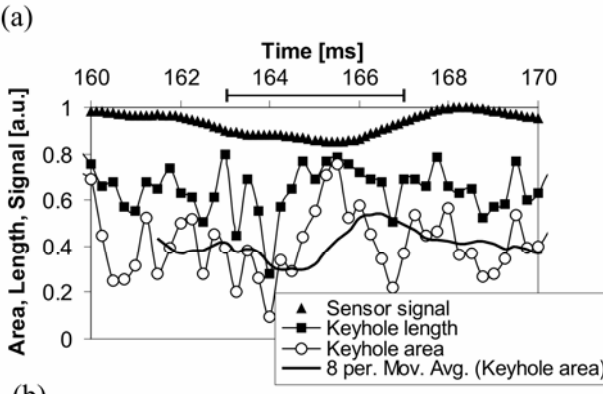
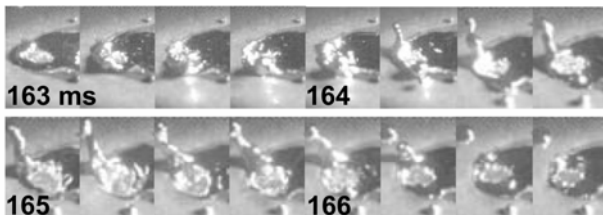


Fig. 10 High speed keyhole dynamics, filtered T-signal

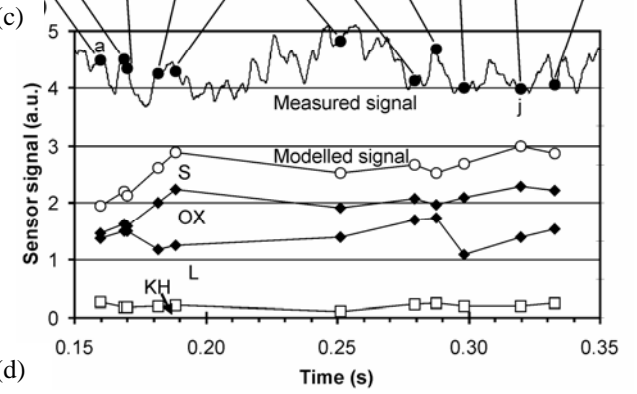
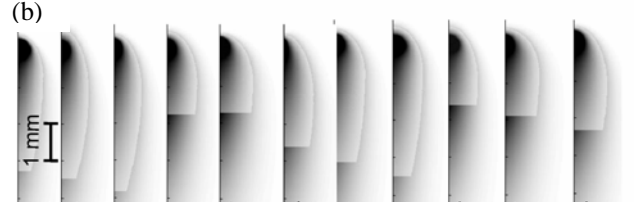
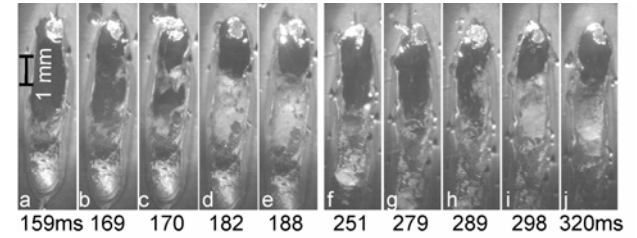
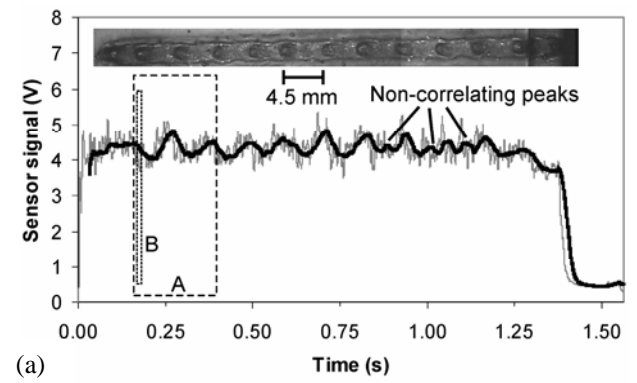
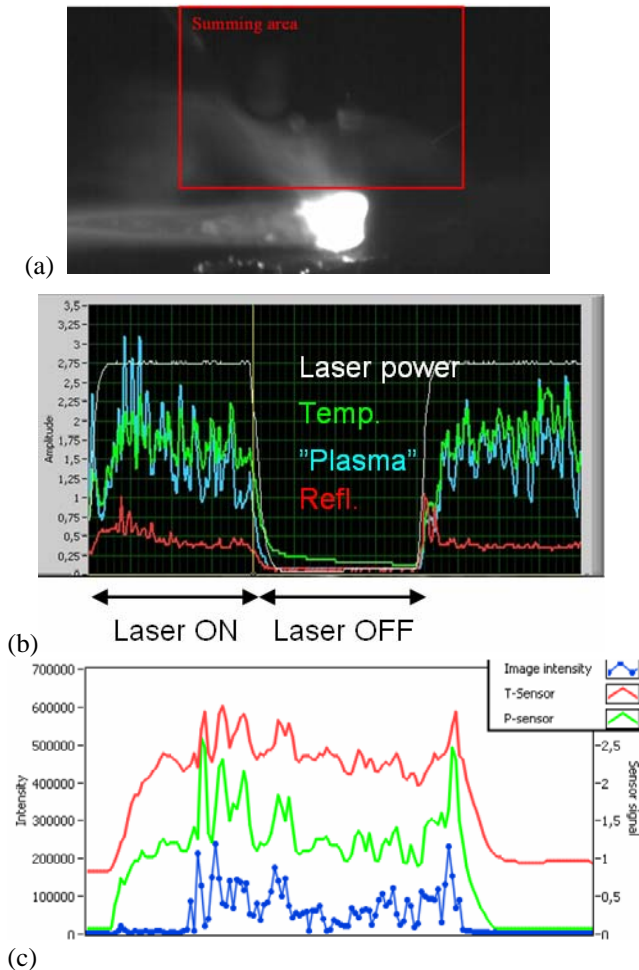


Fig.11 Humping (a) correlation, (b)-(d) analysis 1 period[8]

3.6 Pulsed laser - basic experiment

As monitoring is mainly attributed to dynamic effects but most applications are cw, we also conducted [9] a fundamental pw-welding experiment (Nd:YAG-laser), expecting additional knowledge. Figure 12(a) shows high speed imaging without illumination, thus the vapour plume which was measured with respect to its greyscale (dynamic range of the sensor) content detected in a certain area, as an indicator for the vapour plume radiation. Figure 12(b) shows the acquired P-, T- and R-signals and the pulsed laser power. The T-sensor maintains a significant level during the cooling period, the P-sensor not, giving evidence that the T-sensor reacts much more on moderate temperatures than the P-sensor. However, the peaks of the P- and T-signal coincide almost completely with each other, giving evidence that their origin is the same. When evaluating the vapour plume greyscale by integration over a rectangle (optical path), an integrated value (although non-linear, nevertheless containing information) as a function of time

can be derived, see Fig. 12(c). The peak instants and shape of this curve corresponds well with the T- and P-signals acquired, indicating that the emissive signals (P,T) originate mainly from the vapour radiation, thus the thermal emissions from the melt and solid have less (dynamic) influence. The role of the keyhole is still unclear, as it connects the melt and the metal vapour. However, contributions from the keyhole seem significant and sensitive, too.



**Fig. 12** Base pw-experiment: (a) keyhole with evaluated vapour plume, (b) signal vs. time for the pulsed laser power and the three sensors, (c) comparison of the P- and T-signal with the integrated greyscale of the vapour vs. time.

#### 4. Theoretical description and concluding guidelines

From the different cases studied some of the phenomena responsible for photodiode monitoring of welding defects were better understood. The link between the process dynamics and the photodiode sensors is illustrated in Fig. 13. The T- and P-sensor were most sensitive to the vapour plume dynamics, followed by the keyhole, while the melt pool had much less impact and is therefore more difficult to detect. The important (as resolidifying) rear part of the melt pool can even be located outside the detected (circular) range. The R-sensor is highly sensitive to the keyhole top geometry, providing additional information. High speed phenomena can take place that remain undetected. It is important to be aware of possible filters of the monitoring system that would further lower the detectable dynamics.

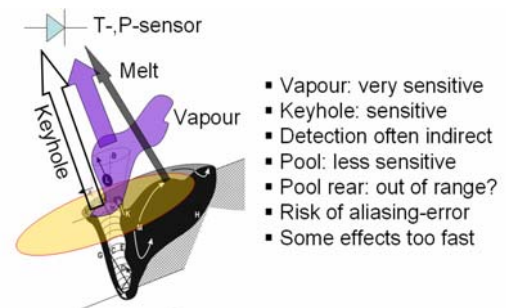


**Fig. 13** Emission link between the process and the sensors

The understanding of the context to judge the potential and limits of photodiode monitoring was partially improved:

- (i) The P- and T-signals were mainly generated from the vapour plume, thus hardly differ in information content
- (ii) The T-signal has an additional temperature component
- (iii) For CO<sub>2</sub>-laser-induced plasma the P-sensor is important
- (iv) The R-sensor offers complementary information to T,P
- (v) Keyhole blowouts but also the melt pool size (width) and humping were well detected, undercut less clearly
- (vi) Several detections are indirect, e.g. root sagging
- (vii) Dynamic melt pool events causing defects can be too fast (> 20 kHz) or outside the detection radius (here: 5 mm)
- (viii) For some geometry-governed mechanisms in- or post-process cameras are favourable to photodiodes: craters generated in the pool, undercut, pores lifting the pool
- (ix) Spatter was difficult to detect with concentric sensors
- (x) More research studies are desirable to accomplish a clearer image of the context process-defect-signal
- (xi) Imaging evaluation and modelling provide improved understanding of the link between process and signal
- (xii) For many applications successful photodiode signal rules were identified; high speed imaging facilitates set-up

#### Acknowledgments

This work was funded by VINNOVA, projects no. 2005-02895, 2006-00563, 2006-00668 (DATLAS, LOST, Fiber-Tube), by the K&A Wallenberg Foundation, project no. KAW2007.0119, and by the Kempe Foundation. The authors are grateful to Precitec KG for support and discussion.

#### References

- [1] J. Petereit, P. Abels, S. Kaierle, C. Kratzsch and E. W. Kreutz: Proc. ICALEO, (2002) 2501.
- [2] J. Shao and Y. Yan: J. Phys.: Conf. Ser., 15 (2005) 101.
- [3] P. Norman, H. Engström and A. F. H. Kaplan: Proc NOLAMP 11, Lappeenranta (FIN), (2007) 273.
- [4] A. F. H. Kaplan, M. Mizutani, S. Katayama and A. Matsunawa: J. Phys. D: Appl. Phys., 35, (2002) 1218.
- [5] P. Norman, J. Karlsson and A. F. H. Kaplan: Proc. LIM, Munich (DE), (2009).
- [6] P. Norman, I. Eriksson and A. F. H. Kaplan: Proc. NOLAMP 12, Copenhagen (DK), (2009).
- [7] A. F. H. Kaplan, E. M. Westin, G. Wiklund and P. Norman: Proc. ICALEO, Temecula (CA), (2008).
- [8] P. Norman, H. Engström and A. F. H. Kaplan: J. Phys. D: Appl. Phys., 41, (2008) 195502.
- [9] I. Eriksson, P. Norman and A. F. H. Kaplan: Proc. NOLAMP 12, Copenhagen (DK), (2009).